



A facile method to conduct 3D self-supporting Co-FeCo/N-doped graphene-like carbon bifunctional electrocatalysts for flexible solid-state zinc air battery

Qiuyan Jin, Bowen Ren, Jianpo Chen, Hao Cui*, Chengxin Wang*

State Key Laboratory of Optoelectronic Materials and Technologies, School of Materials Science and Engineering, The Key Laboratory of Low-Carbon Chemistry & Energy Conservation of Guangdong Province, Sun Yat-sen (Zhongshan) University, Guangzhou 510275, China

ARTICLE INFO

Keywords:

Bifunctional electrocatalyst
Binder-free air-electrode
Nitrogen-doped graphene-like carbon
All-solid-state zinc-air-battery
Flexible electronic

ABSTRACT

The rapid development of wearable and portable electronics is triggering a lot of researches on flexible energy device. Flexible zinc-air batteries (ZABs) with high bifunctional oxygen electrocatalytic activity and superb flexible can be employed as promising power supplies to fulfill these novel electronic devices. Considering the major challenges to the flexible ZABs such as low power density, poor energy efficiency and unsatisfactory mechanical stability, we propose a novel plasma-assistance strategy to prepare highly foldable self-supporting air-electrodes based on nitrogen-doped carbon layer encapsulated Co and FeCo nanoparticles hybrid nanowire arrays (Co-FeCo/N-G). The obtained Co-FeCo/N-G air-electrode show superior oxygen reduction reaction (ORR)/oxygen evolution reaction (OER) activity. Thus, the flexible ZABs using Co-FeCo/N-G air-electrode achieve a high open circuit voltage of 1.419 V. Furthermore, it exhibits an outstanding peak power density of 82 mW cm^{-2} , a small discharge-charge voltage gap of 0.61 V at 1 mA cm^{-2} and long-term durability. Specially, the flexible Co-FeCo/N-G ZAB displays excellent mechanical stability under large deformation conditions, which can be folded into 180° without obvious decay of its performance. Thereby, our work offers a unique insight into design of highly flexible air electrodes with favorable electrocatalytic activity for emerging wearable and portable electronics.

1. Introduction

Flexible electronics, due to their wearable and portable features, have attracted huge attention for practical application such as intelligent bracelets, foldable smart phones and roll-up displays [1–3]. To fully realize these novel electronic devices, suitable power sources with favorable flexibility and high energy density are essential [4,5]. Flexible all-solid zinc-air batteries (ZABs) have been considered as appealing power supplies for wearable/flexible electronics thanks to their high theoretical density (1086 Wh kg^{-1}), flat discharge voltage, low cost and environmental benignity [6–8]. So far, the major challenges to the flexible ZABs are their low power density, poor energy efficiency and unsatisfactory mechanical stability. Their low power density and energy efficiency are primarily caused by the sluggish oxygen reduction reaction (ORR) and oxygen evolution reaction (OER) occurring at flexible air electrodes. Meanwhile, the mechanical stability requires the flexible air electrodes stably operating with deformed shapes. Therefore, an air electrode with superb bifunctional oxygen electrocatalytic

activity and high flex stability is vital to the flexible ZAB.

Nevertheless, most bifunctional active catalysts are in powder form and thus requires ancillary additives (e.g., polymeric binders, carbon black). The use of these additives has some negative impacts on the flexible ZABs [9]. For instance, numbers of active materials are buried during the air-electrodes fabrication, which lowers the performance of the flexible ZABs. The weak adhesion between substrates and electrocatalysts leads to detachment of active materials from the air-electrode surface under frequent or large deformation conditions [10,11]. Thus, it is strongly demanded to develop a novel strategy for realizing physically robust or bendable air-electrodes without ancillary additives.

In the last few decades, various catalysts show promising activity in OER or ORR, such as earth-abundant transition-based metal Co [12,13], Fe [14,15], Ni [16,17]. Previous researches have shown that Co-based catalysts possess high OER activity [18–20]. Meanwhile, Fe-N-C materials, which are comparable to the Pt/C, can efficiently catalyze the ORR process [21–23]. Because of synergistic metal-interactions, adding heteroatom Fe into Co-based materials is likely to obtain bifunctional

* Corresponding authors.

E-mail addresses: cuihao3@mail.sysu.edu.cn (H. Cui), wchengx@mail.sysu.edu.cn (C. Wang).

<https://doi.org/10.1016/j.apcatb.2019.117887>

Received 10 April 2019; Received in revised form 11 June 2019; Accepted 18 June 2019

Available online 19 June 2019

0926-3373/© 2019 Elsevier B.V. All rights reserved.

catalysts with high activity [24]. Moreover, carbon materials (graphene, carbon nanotubes, etc.) are considered as active catalysts by nitrogen doping to tune their chemical and electronic properties. The graphene with nitrogen doping exhibits improved bifunctional catalytic activity [25–28]. And both oxygen activity of transition metal (Co and Fe) combined with the nitrogen-doped carbon may be further enhanced, because of the synergistic effect between them.

Inspired by the aforementioned considerations, we proposed a novel plasma-assisted process to prepare highly bendable free-standing air-electrodes based on nitrogen-doped carbon layer encapsulated Co and FeCo nanoparticles hybrid nanowires (Co-FeCo/N-G) for the flexible ZABs. The Co-FeCo/N-G nanowire array on flexible carbon cloth (CC) was obtained by directly treating the FeCo hydroxide precursor using the novel NH_3 and CH_4 plasmas with short duration (10 min). NH_3 and CH_4 plasmas, served as efficient nitrogen and carbon sources, can provide highly reactive environment and fast preparation [29,30]. Specially, the etching effect of the plasma endows the Co-FeCo/N-G nanowire array with porosity and thus exposes more active sites. Notably, the porous self-supporting Co-FeCo/N-G air-electrode shows remarkable OER and ORR activity. As a proof of concept, a flexible additive-free ZAB using the Co-FeCo/N-G air-electrode offer an outstanding peak power density of 82 mW cm^{-2} , reliable cycling performance with a small charge-discharge gap of 0.61 V and superior stability. More importantly, the flexible Co-FeCo/N-G ZAB can work without losing its performance under the mechanical stress, especially in frequent or large deformation conditions.

2. Experimental section

2.1. Materials

All reagents were directly used without further purification. Cobalt nitrate hexahydrate ($\text{Co}(\text{NO}_3)_2 \cdot 6\text{H}_2\text{O}$), ferrous nitrate hexahydrate ($\text{Fe}(\text{NO}_3)_3 \cdot 9\text{H}_2\text{O}$), ammonium, fluoride (NH_4F), urea ($\text{CO}(\text{NH}_2)_2$), acrylic acid ($\text{C}_3\text{H}_4\text{O}_2$), N,N' -methylene-bisacrylamide ($\text{C}_7\text{H}_{10}\text{N}_2\text{O}_2$) and ammonium persulfate ($(\text{NH}_4)_2\text{S}_2\text{O}_8$) were purchased from Aladdin, potassium hydroxide (KOH) was purchased from Sinopharm Chemical Reagent.

2.2. Pretreatment of carbon cloth

A piece of carbon cloth was soaked in concentrated sulfuric acid (H_2SO_4 , 98%) overnight and then ultrasonicated for 15 min in ethanol solution. Finally, the carbon cloth was washed by deionized water several times.

2.3. Synthesis of FeCo and Co nanowires precursor on carbon cloth

FeCo precursor nanowires directly grown on carbon cloth were prepared as following: 1 mmol of $\text{Fe}(\text{NO}_3)_3 \cdot 9\text{H}_2\text{O}$, 2 mmol of $\text{Co}(\text{NO}_3)_2 \cdot 6\text{H}_2\text{O}$, 4 mmol of NH_4F and 10 mmol of $\text{CO}(\text{NH}_2)_2$ were dissolved in 35 ml deionized water with 30 min of violent stirring to obtain a pink solution. The mixed solution and a piece of pretreated carbon cloth were transferred to Teflon-lined stainless-steel autoclave (50 ml), and then the autoclave was sealed and heated at 120°C for 6 h.

For comparison, the Co precursor nanowires was prepared as following: 3 mmol of $\text{Co}(\text{NO}_3)_2 \cdot 6\text{H}_2\text{O}$, 4 mmol of NH_4F and 10 mmol of $\text{CO}(\text{NH}_2)_2$ were dissolved in 35 ml deionized water under 30 min violent stirring. The next processing step using the same method as Co-FeCo precursors.

2.4. Synthesis of porous Co-FeCo/N-G, Co/N-G structures on carbon cloth

The as-prepared Co-FeCo and Co precursor nanowires converted into Co-FeCo/N-G and Co/N-G structures by microwave plasma enhanced chemical vapor deposition system (MPECVD). The rectangular

microwave waveguide couples the microwave power in a quartz tube, which generated the plasma. The Co-FeCo/Co nanowire precursor was placed in the reaction chamber. The MPECVD system was evacuated to 2 m Torr, then the CH_4 , H_2 and NH_3 gas flowed into the reaction chamber at a flow rate of 10 sccm, 20 sccm, 10 sccm, respectively. Plasma was generated at 1000 W for 10 min with a base pressure of 10 Torr.

2.5. Synthesis of porous Co-FeCo/G and bare Co-FeCo structures on carbon cloth

The synthetic process of Co-FeCo/G was similar with that of Co-FeCo/N-G except the introduction of ammonia gas. The synthetic process of bare Co-FeCo nanowires was similar with that of Co-FeCo/N-G. The bare Co-FeCo nanowires is obtained by directly treating the FeCo hydroxide precursors only with H_2 plasma.

2.6. Materials characterizations

XRD patterns were obtained by X-ray diffraction (XRD) (Rigaku X-ray diffractometer D-MAX 2200 VPC) using Cu $\text{K}\alpha$ radiation ($\lambda = 0.15418 \text{ nm}$) with a scanning step size of $10^\circ (\text{s}^{-1})$. The morphologies of samples were characterized by a scanning electron microscopy (SEM, Carl Zeiss, Auriga-4525) at an acceleration voltage of 5 kV and 10 kV. TEM and HRTEM images were taken on a FEI Tecnai G2 F30 microscope operated at 300 kV. X-ray photoelectron spectroscopy (XPS) measurements were performed using an ESCA Lab250 spectrometer using a twin-anode Al $\text{K}\alpha$ (1486.6 eV) X-ray source. Energy Dispersive Spectrometer (SEM-EDS, Carl Zeiss, Auriga-4525) was carried out to calculate the atom percentage of elements.

2.7. Electrochemical measurements

The electrochemical measurements were performed in a three-electrode configuration at room temperature. Data were collected in a standard three-electrode system with Bio-logic VMP3 electrochemical workstation. A Hg/HgO electrode and a graphite rod served as the reference electrode and counter electrode, respectively. The samples were directly used as working electrodes. OER performances were tested in 1 M KOH solution, while ORR performances were tested in O_2 -saturated 0.1 KOH electrolyte. All recorded potentials were calibrated to the reversible hydrogen electrode (RHE) using the Nernst equation: $E_{\text{RHE}} = E_{\text{Hg/HgO}} + 0.059 \times \text{pH} + 0.098$. Electrochemical impedance spectroscopy (EIS) for OER was performed over a frequency range from 100 kHz to 0.01 Hz at overpotential of 1.56 V vs RHE with an amplitude of 10 mV.

2.8. Assembly of flexible all-solid-state Zn-air battery

The flexible Zn-air battery was fabricated in a sandwich structure. A zinc foil, Co-FeCo/N-G free-standing film and gel were employed as anode, cathode and solid electrolyte. The gel was coated on the Zn foil and Co-FeCo/N-G cathode was attached to the other side of gel.

The gel electrolyte was manufactured as follow: A mixture solution containing 11.25 M KOH and 0.25 M ZnO was prepared. Then, 0.08 g N, N' -methylene-bisacrylamide and 480 μL acrylic acid were added in the mixing solution with violent stirring. Five minutes later, the white precipitate was filtered out and the solution was poured onto a glass plate. Then, 30 μL of 0.3 M ammonium persulfate was added to the solution. The gel was obtained after several minutes of polymerized at room temperature.

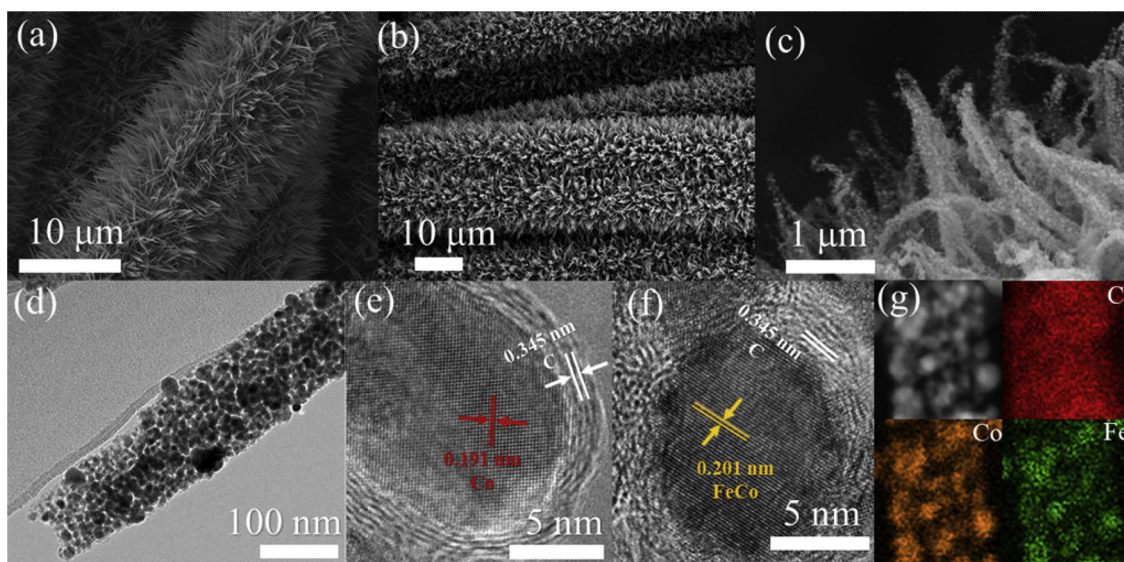


Fig. 1. (a) SEM image of FeCo precursor nanowires (b) Low magnification SEM image of Co-FeCo/N-G needle-like structures (c) High magnification SEM image of Co-FeCo/N-G needle-like structures (d) TEM image of Co-FeCo/N-G needle-like structures (e) HR-TEM image of cobalt nanoparticle in Co-FeCo/N-G. (f) HR-TEM image of FeCo alloy nanoparticle in Co-FeCo/N-G. (g) elemental mapping images of Co-FeCo/N-G: carbon (red), cobalt (yellow) and iron (green). (For interpretation of the references to colour in this figure legend, the reader is referred to the web version of this article).

3. Results and discussion

3.1. Synthesis, structure, and composition of materials

Scanning electron microscopy (SEM) image shows that FeCo precursor nanowire arrays with smooth surface are uniformly distributed on carbon cloth (Fig. 1a and Fig. S1). After rapid plasma-assistant treatment, the nanowire structures are still maintained well (Fig. 1b). These needle-like structures attach closely to the substrate, favoring long-term durability and efficient electron transport of the electrocatalysts [31]. As shown in high-magnification SEM image, the surface of these nanowires become rough (Fig. 1c). Further, the transmission electron microscopy (TEM) image reveals that the nanowires consist of small nanoparticles (Fig. 1d) and possess abundant pore structures (Fig. S2). The pores make sure the more nanoparticles directly contact with electrolyte and thus accelerate the charge transfer and diffusion between them, which is beneficial to the performance of catalysts [32]. More details about the nanoparticles are demonstrated by high-resolution TEM (HRTEM). The nanoparticles are divided into two types: metallic cobalt and iron-cobalt alloy. Lattice fringe spaces of 0.191 nm are attributed to the (101) planes of metal cobalt (Fig. 1e.), and the adjacent-planes of 0.201 nm are assigned to the (110) planes of FeCo alloy (Fig. 1f.). Both Co and FeCo nanoparticles are encapsulated by few carbon layer with lattice spacings of 0.345 nm. Moreover, the distribution of Fe, Co and C elements is illustrated by energy filtered TEM (EFTEM) mapping (Fig. 1g). The C elements are distributed in the whole nanowire, forming the framework of the nanowire. Co and Fe elements are mainly concentrated on nanoparticles. TEM results demonstrate that the porous nanowires consist of carbon-packed metal Co and bimetal FeCo nanoparticles.

XRD patterns further verify the coexistence of FeCo and Co in the Co-FeCo/N-G sample. As shown in Fig. 2a, the diffraction peaks of metal cobalt are detected at 41.6°, 44.2°, 47.5°, 51.5° and 75.8° (PDF#05-0727 and PDF #15-0806). The diffraction peaks appeared at 44.8° and 82.7° match well with the (110) and (200) crystal facets of FeCo alloy (PDF#49-1568). Hence, hydroxide precursors (Fig. S3) are completely transformed into metallic Co/FeCo. To give a quantitative analysis of metal Co and bimetal FeCo nanoparticles, we carried out Energy Dispersive Spectrometer (EDS) to calculate the atom percentage of elements in Co-FeCo/N-G (Fig. S4a). Based on the atom percentage,

Co-FeCo/N-G contains 65.95, 2.85, 0.67, 8.59 and 21.94 at% of C, N, O, Fe and Co, respectively (Fig. S4b). According to the atom percentage of Co and Fe species, the atomic ratio of Co/FeCo is 1.55. The surface chemical binding states of elements are identified by X-ray photoelectron spectroscopy (XPS). The survey XPS spectrum of Co-FeCo/N-G further exhibits the presence of C, N, O, Co and Fe species (Fig. S5). The C1s spectrum (Fig. 2b) ensures the existence of C–C (284.8 eV), C=O (286.6 eV) and π - π^* (291.3 eV) bonds [33]. Meanwhile, the C–N is observed at 285.4 eV, indicating that the N species are incorporated into Carbon skeleton. N incorporation is also evidenced by graphitic N (401.1 eV) in the N 1s spectrum (Fig. 2c) [34]. And the pyridinic N centered at 398.6 eV in N 1s implies the presence of metal–N bonds [35]. The bonding status of Co in Co-FeCo/N-G is analyzed by the high-resolution Co 2p spectrum (Fig. 2d), the sharp peaks centered at 778.5 eV and 793.6 eV are deemed as cobalt with zero-valence state, which corresponds to metallic cobalt in elemental Co and FeCo alloy [36]. The weak peaks at around 780.1 eV and 782.5 eV can be indexed to the Co^{3+} and Co^{2+} species, respectively [37]. Similarly, Fe 2p spectrum exhibits Fe with zero-valence state (707.4 eV and 720.1 eV) in Fig. 2e, which is derived from FeCo alloy. The deconvoluted peaks at around 713.1 eV and 710.9 eV are assigned to Fe^{3+} species and Fe^{2+} species [38–40]. And the presence of high-valence state species may be ascribed to the oxidation of sample in atmosphere. The XPS spectrums for two comparisons of Co/N-G and Co-FeCo/G are also performed for comparative analysis. The Co/N-G nanowires were synthesized without adding Fe sources in hydroxide precursors and the Co-FeCo/G nanowires were prepared without introduction of NH_3 plasma (more details see Fig. S6–S8 and experimental section). As shown in Fig. S9a, there are C–C, C=O, C–N and π - π^* bonds in the C 1s XPS spectra of Co/N-G. In contrast to the samples with N-doping (Co/N-G and Co-FeCo/N-G), the signal of C–N bond is not detected in the C 1s spectra of Co-FeCo/G, demonstrating that N incorporation in Co-FeCo/N-G and Co/N-G is derived from NH_3 during plasma-assisted process. The result is further confirmed by N 1s XPS spectra. As shown in Fig. S9b, the peak at 401.1 eV and 398.6 eV correspond to graphitic N and pyridinic N in N 1s XPS spectra of Co/N-G, respectively. On the contrast, the peak for N species is invisible in Co-FeCo/G. Co 2p spectra shows the coexistence of Co^0 , Co^{2+} and Co^{3+} in both Co/N-G and Co-FeCo/G, which is in accordance with Co-FeCo/N-G (Fig. S9c). Similarly, Fe 2p spectra shows the bonding states of Fe species in Co-FeCo/G is consistent to that in Co-

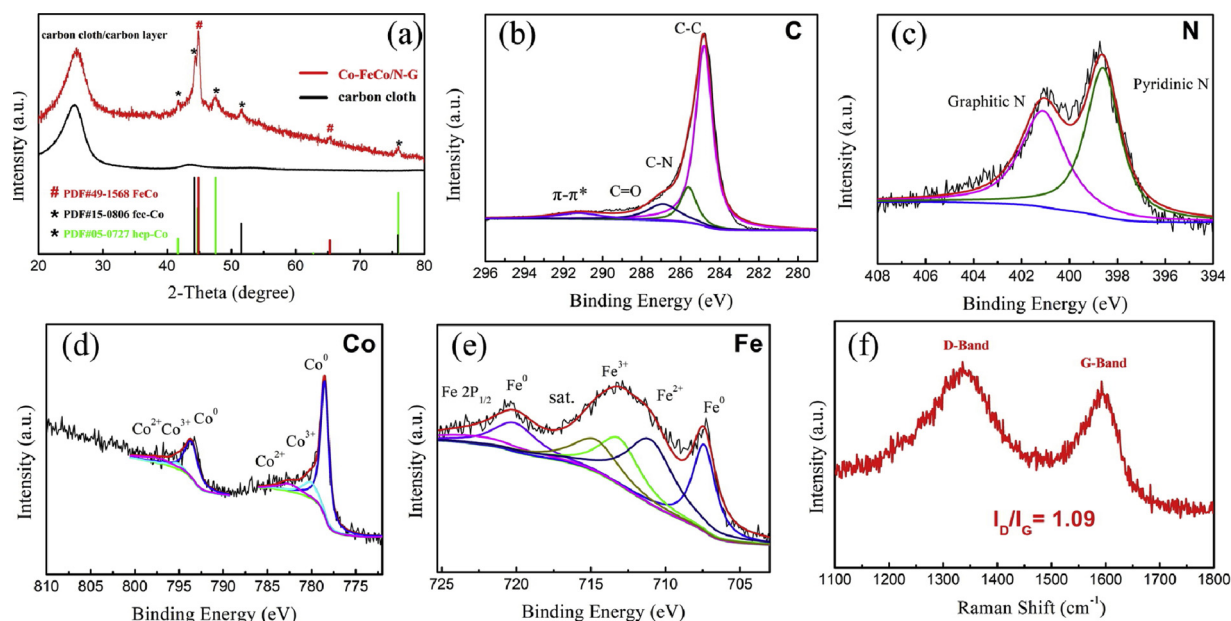


Fig. 2. (a) XRD pattern of Co-FeCo/N-G. XPS spectra of (b) C 1s (c) N 1s (d) Co 2p (e) Fe 2p of Co-FeCo/N-G. (f) Raman spectra of Co-FeCo/N-G.

FeCo/N-G (Fig. S9d). Besides, Raman spectroscopy can be employed to reveal the structure defects. The Raman spectrum of Co-FeCo/N-G is exhibited in Fig. 2f, the D- band at 1335 cm^{-1} represents defects and disorder, and the G- band at 1594 cm^{-1} refers to a stretching vibration in the plane of sp^2 hybridized C atoms [26,41,42]. Therefore, intensity ratio of the D- and G- band (I_D/I_G) in our work is 1.09, indicating that there are some defects in the surface carbon layer of Co-FeCo/N-G nanowires.

3.2. Electrochemical properties of catalysts

In order to explain the significant function of the incorporation of Fe and N species, the free-standing Co-FeCo/N-G, Co/N-G and Co-FeCo/G were directly utilized as working electrode to assess their bifunctional catalytic activity. The catalytic ability of samples toward OER was investigated in 1 M KOH solution at 25°C . All LSV data for OER are reported with 90% IR compensation to fairly compare the performance of catalysts. As shown in Fig. 3a, the Co/N-G nanowires require an overpotential of 310 mV to drive a current density of 10 mA cm^{-2} . Impressively, Co-FeCo/N-G exhibit a significantly enhanced OER performance because of incorporation of Fe species and it only offer an overpotential of 258 mV to drive a current density of 10 mA cm^{-2} . Meanwhile, the OER performance of Co-FeCo/N-G also superior to that of Co-FeCo/G (318 mV), meaning that the introduction of N elements is also in favor of improving catalytic activity for OER. It is worth noting that the Co-FeCo/N-G at a small overpotential of 330 mV can deliver a current density of 300 mA cm^{-2} , which is one order of magnitude higher than Co/N-G (18 mA cm^{-2}) and Co-FeCo/G (16 mA cm^{-2}). The improved OER performance of Co-FeCo/N-G is derived from the synergistic effect among Co, FeCo, and N doped graphene-like carbon. Tafel slopes are employed to analyze the reaction kinetics for OER. Tafel slopes of 70 mV dec^{-1} , 41 mV dec^{-1} and 34 mV dec^{-1} are obtained for Co/N-G, Co-FeCo/G and Co-FeCo/N-G in Fig. 3b, respectively. Clearly, Co-FeCo/N-G exhibits a fast OER kinetic process with the lowest Tafel slope, which is in accordance with the electrochemical impedance spectroscopy (EIS) analysis (Fig. S10). The R_{ct} of samples follows the order: Co/N-G ($7.764\ \Omega$) > Co-FeCo/G ($4.397\ \Omega$) > Co-FeCo/N-G ($0.405\ \Omega$). The R_{ct} of Co-FeCo/N-G from the Nyquist plot's pattern is the smallest during the OER process, indicating a more efficient electron transport at the Co-FeCo/N-G-electrolyte interface. Previous work demonstrates the existence of Fe may influence the redox

properties of Co, leading to a partial-charge transfer activation effect on Co and thus the OER activity of Co-based catalysts is improved [43,44]. Then, the stability of Co-FeCo/N-G for OER was examined by continuous cycling with 5000 cyclic voltammetry cycles. The results show that Co-FeCo/N-G can retain stable catalytic activity after 5000 cycles (Fig. S11). Chronopotentiometry was also employed to test the stability of Co-FeCo/N-G and there is no obvious performance decay during continuous operation of 20 h with 10 mA cm^{-2} , suggesting the as prepared Co-FeCo/N-G nanowires are highly durable electrocatalysts for OER (Fig. 3c). We further collect the cycling voltammetry data (Fig. S12) to estimate their electrochemical double-layer capacitance (C_{dl}), which is proportional to the electrochemically active surface area (ECSA). As shown in Fig. 3d, the C_{dl} of Co-FeCo/N-G (39.9 mF cm^{-2}) is about double that of Co/N-G (23.8 mF cm^{-2}) but around eight times Co-FeCo/G (5.5 mF cm^{-2}), revealing that more exposed active sites and higher electrochemically surface area in Co-FeCo/N-G nanowires.

Likewise, Co-FeCo/N-G nanowire array was also directly used as the working electrode for the measurements toward ORR. The CV curves of Co-FeCo/N-G were tested in a N_2 - or O_2 -saturated 0.1 M KOH electrolyte at a scan rate of 10 mV s^{-1} . As shown in Fig. 3e, in comparison with the electrochemical response in N_2 -saturated solution, an apparent cathodic peak at around 0.77 V versus RHE is observed for the Co-FeCo/N-G nanowires in O_2 -saturated KOH solution, which is superior to that of Co/N-G and Co-FeCo/G (Fig. S13); The LSV curves further indicate the higher ORR activity of the Co-FeCo/N-G nanowires (Fig. 3f). The onset potentials are 0.89 V, 0.87 V and 0.82 V for ORR on Co-FeCo/N-G, Co/N-G and Co-FeCo/G, respectively. Meanwhile, the half-wave potential of samples follows the order: Co-FeCo/N-G (0.82 V) > Co/N-G (0.80 V) > Co-FeCo/G (0.74 V). Obviously, the Co-FeCo/N-G nanowires possess the best electrocatalytic activity for ORR, which is also confirmed by diffusion-limited current densities. Similarly, Co-FeCo/N-G nanowires provide the largest diffusion-limited current densities. For instance, the diffusion-limited current densities of Co-FeCo/N-G, Co/N-G and Co-FeCo/G are -2.28 mA cm^{-2} , -1.76 mA cm^{-2} and -1.57 mA cm^{-2} at 0.5 V, respectively. All these results demonstrate that ORR activity of Co-FeCo/N-G nanowires is greatly improved through the introduction of both Fe and N species. Then, the ORR cycle stability of Co-FeCo/N-G was examined. The polarization curves for ORR were collected before and after 5000 cycles. The voltammetric behavior of the Co-FeCo/N-G catalyst differs slightly (Fig. S14). After 5000 continuous cycles, the results show a negligible loss of 10 mV in the half-wave potential for

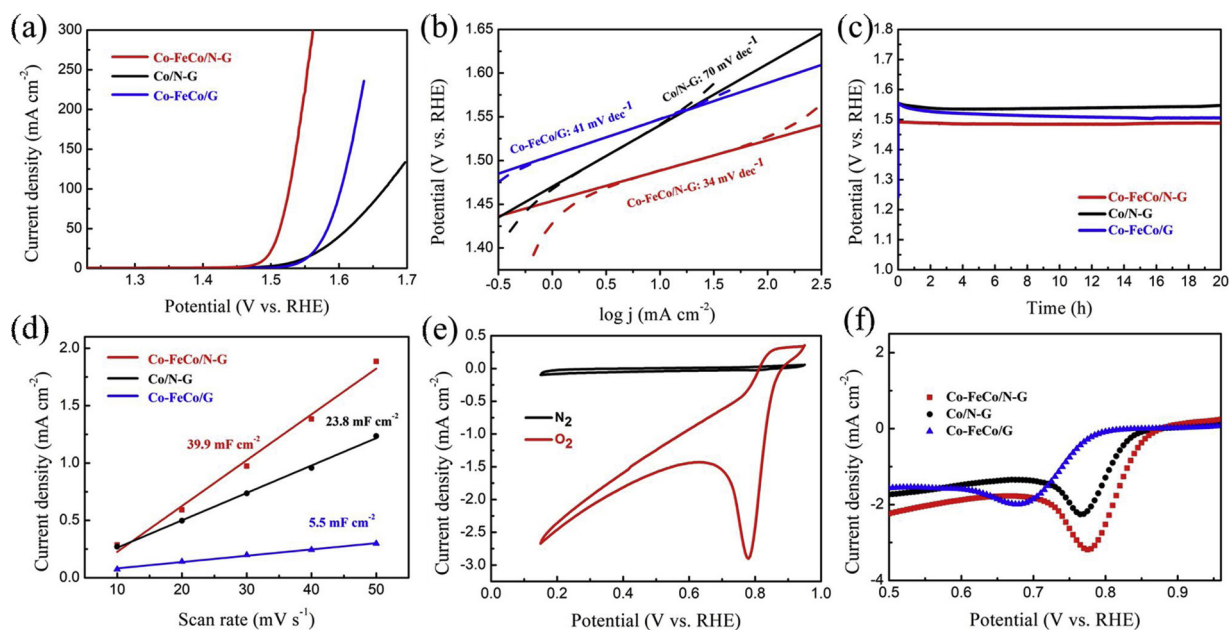


Fig. 3. (a) Polarization curves of Co-FeCo/N-G, Co/N-G and Co-FeCo/G in 1 M KOH with a scan rate of 2 mV s^{-1} . (b) Tafel plots of Co-FeCo/N-G, Co/N-G and Co-FeCo/G. (c) long-term OER stability test (without iR corrected) of Co-FeCo/N-G, Co/N-G and Co-FeCo/G. (d) The double-layer charging current density difference plotted as a function of scan rate fitted to a linear regression. (e) CV curves of the Co-FeCo/N-G measured in both N_2 -saturated and O_2 -saturated 0.1 M KOH. (f) LSV curves of Co-FeCo/N-G, Co/N-G and Co-FeCo/G for ORR in O_2 -saturated 0.1 M KOH.

Co-FeCo/N-G, which indicates Co-FeCo/N-G also possess favorable ORR stability. Additionally, to illustrate the encapsulation of N-doped carbon on Co and FeCo nanoparticles is in favor of bifunctional catalytic activity of Co-FeCo/N-G, we also prepared bare Co-FeCo nanowires and further assessed the bifunctional electrocatalytic activity of bare Co-FeCo. (details see the caption of Fig. S15).

3.3. Flexible all-solid-state Zn-air battery measures

The robust ORR and OER electrocatalytic performances of Co-FeCo/N-G electrode make it hold great promise for future energy application. To satisfy increasing demand for wearable electronic device, flexible Zn-air battery (ZAB) was assembled using Co-FeCo/N-G electrode as cathode, Zn foil as anode and hydrogel electrolyte. As shown in Fig. 4a, the ZAB assembled with Co-FeCo/N-G exhibits an open-circuit voltage of 1.419 V. Fig. 4b depict its polarization and power density curves for different samples under atmospheric air. Obviously, the Co-FeCo/N-G ZAB produces a larger voltage than the Co/N-G ZAB and Co-FeCo/G ZAB under the same current density, which is consistent to the half-cell ORR measurement. It is noting that Co-FeCo/N-G ZAB can deliver a much higher peak power density of 82 mW cm^{-2} compared to that of Co/N-G ZAB (56 mW cm^{-2}) and Co-FeCo/G ZAB (25 mW cm^{-2}). The charge polarization curves of Co-FeCo/N-G ZAB also exhibit in Fig. S16. Moreover, the galvanostatic discharge tests at various current densities from 1 mA cm^{-2} to 20 mA cm^{-2} are showed in Fig. 4c. Impressively, the Co-FeCo/N-G ZAB delivers a high discharge voltage at each current density. For instance, even at a high current density of 20 mA cm^{-2} , the discharge voltage for the Co-FeCo/N-G ZAB is 1.12 V, whereas the discharge voltage for the Co/N-G ZAB and Co-FeCo/G ZAB are 0.877 V and 0.738 V, respectively. The above results indicate the enhanced ORR performance of the Co-FeCo/N-G ZAB and highlight the important function of introduction of both Fe and N species in catalytic activity. Additionally, the flexible ZAB using Co-FeCo/N-G as the air cathode can operate for 2.4 h at a current density of 10 mA cm^{-2} (inset of Fig. S17). Figure S17 shows the specific discharging capacity of the flexible ZAB is 609 mA h g^{-1} at a current density of 10 mA cm^{-2} . The galvanostatic discharge and charge profiles at a current density of 1 mA cm^{-2} with each cycle being 10 min (5 min for discharging and the 5 min for

charging) is further employed to investigate the cycling performance (Fig. 4d). Notably, the Co-FeCo/N-G ZAB produce a high initial discharge potential of 1.30 V and a charge potential of 1.91 V, with a small voltage gap of 0.61 V at 1 mA cm^{-2} , which are better than that of Co/N-G ZAB and Co-FeCo/G ZAB (Fig. 4e). After continuous 18 h operation, the voltage gap only slightly increase 0.12 V and the Co-FeCo/N-G ZAB still maintain flat charging/discharging platforms compared to the Co/N-G ZAB or Co-FeCo/G ZAB (Fig. 4f), suggesting the superior battery durability of ZAB using Co-FeCo/N-G as the air cathode. The galvanostatic discharge and charge profiles for Co-FeCo/N-G ZAB at a current density of 2 mA cm^{-2} are showed in Fig. S18 and the cycling performance is also competitive (1.27 V and 1.92 V for discharging and charging with a small voltage gap of 0.7 V), which is among the best values for flexible all-solid-state ZAB. The ZAB battery based on Co-FeCo/N-G with the outstanding catalytic activity and superior rechargeability displays potential application for flexible and wearable electronic device.

To explore how well the catalyst meets the requirements for practical applications of flexible device, we continue to test circling performance of the Co-FeCo/N-G ZAB under the bending condition. Clearly, the Co-FeCo/N-G ZAB can be folded into various degree even 180° with almost unchanged discharging/charging performance (Fig. 5a). Then, the 180° -folded Co-FeCo/N-G ZAB recovers to initial degree (0°), the battery performance is also not influenced. We further tested the circling performance of Co-FeCo/N-G ZAB under the bending condition for a longer time. As shown in Fig. S19a, the Co-FeCo/N-G ZAB can stably operate in a 90° -folded state for 30,000 s. And the Co-FeCo/N-G ZAB is bent to 180° , it also exhibits favorable circling performance and stability (Fig. S19b). Furthermore, we can see that the Co-FeCo/N-G ZAB powers LEDs with different colors under both unfolded (Fig. 5b) and folded condition (Fig. 5c). The favorable flexible nature of Co-FeCo/N-G ZAB should be primarily due to the strong adhesion of catalysts and substrates in binder-free Co-FeCo/N-G air electrode, which avoid the detachment of active materials from the CC under the large deformation conditions. Thereby, the results prove that the flexible Co-FeCo/N-G ZAB holds great potential for application in wearable/flexible electronics field.

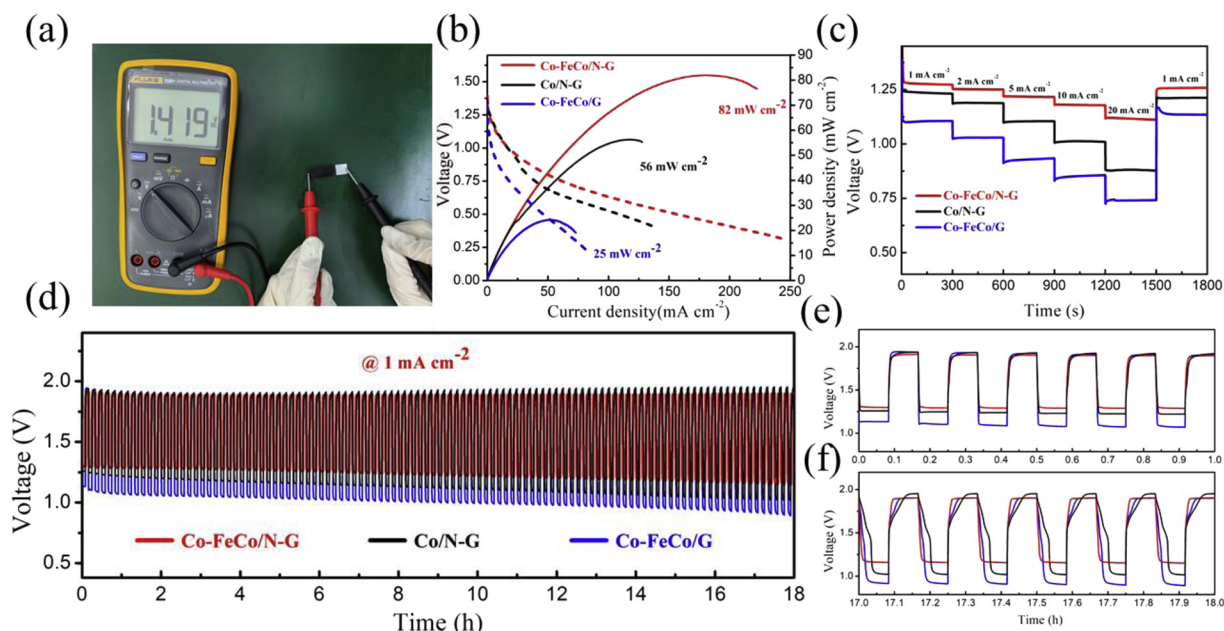


Fig. 4. (a) Open circuit voltage of the flexible ZAB using Co-FeCo/N-G nanowire. (b) discharge polarization and the corresponding power density curves of the Co-FeCo/N-G ZAB, Co/N-G ZAB and Co-FeCo/G ZAB. (c) Galvanostatic discharge of Co-FeCo/N-G ZAB, Co/N-G ZAB and Co-FeCo/G ZAB with different current densities. (d) Galvanostatic charge-discharge profile of the Co-FeCo/N-G ZAB, Co/N-G ZAB and Co-FeCo/G ZAB. (e) The first hour and (f) the last hour of enlarged Galvanostatic charge-discharge profile of Co-FeCo/N-G ZAB, Co/N-G ZAB and Co-FeCo/G ZAB.

4. Conclusion

In summary, we have reported a novel NH₃ and CH₄ plasma-assisted process to prepare the highly bendable additive-free air electrode with superb bifunctional activity for flexible ZAB, which is realized by porous Co-FeCo/N-G nanowires electrocatalysts directly grown on the CC. Compared to the electrocatalysts without N doping (Co-FeCo/G) or introduction of Fe species (Co/N-G), the Co-FeCo/N-G exhibits the enhanced bifunctional catalytic activity, indicating that the incorporation of both Fe and N are in favor of the OER/ORR activity. Meanwhile, the etching effect of plasma endows the Co-FeCo/N-G nanowires with porous structures and thus exposes more active sites. These improved properties ensure the excellent battery performance of the flexible ZAB based on Co-FeCo/N-G air electrode. Moreover, due to the strong

adhesion of catalysts and substrates in additive-free air electrode, assembled flexible Co-FeCo/N-G ZAB can work at large mechanical deformation without obvious decay of performance. Thereby, our work displays a facile strategy to construct favorable flexible air electrode with superb electrocatalytic activity for emerging wearable and portable electronics. This facile synthetic route is expected to offer an efficient design of highly foldable air electrode with outstanding electrocatalytic activity for flexible ZAB and facilitate the implementation of flexible technologies and wearable electronics.

Acknowledgements

This work was financially supported by the National Natural Science Foundation of China (Grants Nos. 51772338 and U1801255)

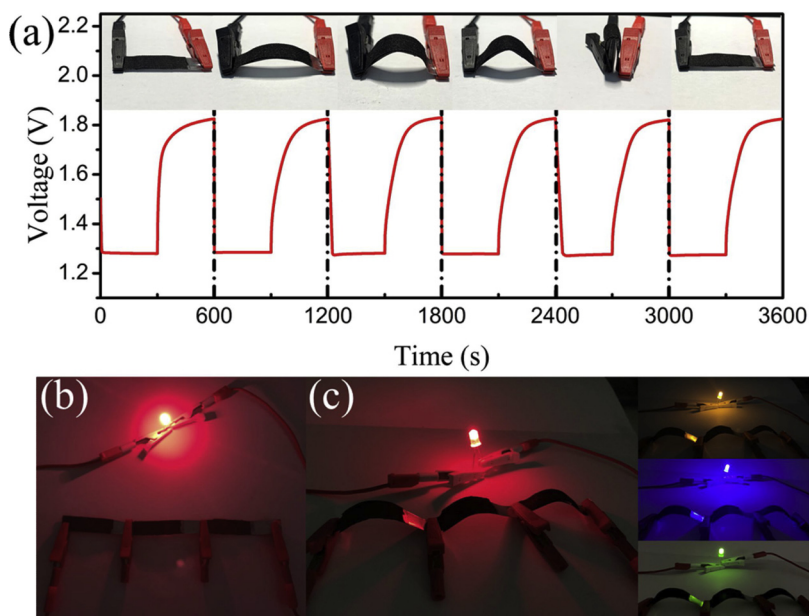


Fig. 5. (a) Cyclic stability of Co-FeCo/N-G ZAB under different bending states at 1 mA cm⁻². (b) Red LED powered by Co-FeCo/N-G ZABs in series. (c) LEDs with different colors powered by Co-FeCo/N-G ZABs in series under bending states. (For interpretation of the references to colour in this figure legend, the reader is referred to the web version of this article).

Appendix A. Supplementary data

Supplementary material related to this article can be found, in the online version, at doi:<https://doi.org/10.1016/j.apcatb.2019.117887>.

References

- [1] J. Zhang, J. Fu, X. Song, G. Jiang, H. Zarrin, P. Xu, K. Li, A. Yu, Z. Chen, *Adv. Energy Mater.* 6 (2016) 1600476.
- [2] H. Nishide, K. Oyaizu, *Science* 319 (2008) 737–738.
- [3] W. Liu, K. Feng, Y. Zhang, T. Yu, L. Han, G. Lui, M. Li, G. Chiu, P. Fung, A. Yu, *Nano Energy* 34 (2017) 491–499.
- [4] J. Park, M. Park, G. Nam, J.-s. Lee, J. Cho, *Adv. Mater.* 27 (2015) 1396–1401.
- [5] D. Ji, L. Fan, L. Li, S. Peng, D. Yu, J. Song, S. Ramakrishna, S. Guo, *Adv. Mater.* (2019) 1808267.
- [6] Z.-Q. Liu, H. Cheng, N. Li, T.Y. Ma, Y.-Z. Su, *Adv. Mater.* 28 (2016) 3777–3784.
- [7] J.-S. Lee, S. Tai Kim, R. Cao, N.-S. Choi, M. Liu, K.T. Lee, J. Cho, *Adv. Energy Mater.* 1 (2011) 34–50.
- [8] Y. Li, H. Dai, *Chem. Soc. Rev.* 43 (2014) 5257–5275.
- [9] K. Kordek, L. Jiang, K. Fan, Z. Zhu, L. Xu, M. Al-Mamun, Y. Dou, S. Chen, P. Liu, H. Yin, P. Rutkowski, H. Zhao, *Adv. Energy Mater.* 9 (2019) 1802936.
- [10] J. Fu, Z.P. Cano, M.G. Park, A. Yu, M. Fowler, Z. Chen, *Adv. Mater.* 29 (2017) 1604685.
- [11] X. Chen, B. Liu, C. Zhong, Z. Liu, J. Liu, L. Ma, Y. Deng, X. Han, T. Wu, W. Hu, J. Lu, *Adv. Energy Mater.* 7 (2017) 1700779.
- [12] X. Lyu, G. Li, X. Chen, B. Shi, J. Liu, L. Zhuang, Y. Jia, *Small Methods*. (2019), <https://doi.org/10.1002/smt.201800450>.
- [13] M. Zeng, Y. Liu, F. Zhao, K. Nie, N. Han, X. Wang, W. Huang, X. Song, J. Zhong, Y. Li, *Adv. Funct. Mater.* 26 (2016) 4397–4404.
- [14] Y. Hou, T. Huang, Z. Wen, S. Mao, S. Cui, J. Chen, *Adv. Energy Mater.* 4 (2014) 1400337.
- [15] Q. Wang, Y. Lei, Z. Chen, N. Wu, Y. Wang, B. Wang, Y. Wang, J. Mater. Chem. A. 6 (2018) 516–526.
- [16] W. Wan, X. Liu, H. Li, X. Peng, D. Xi, J. Luo, *Appl. Catal. B* 240 (2019) 193–200.
- [17] X.-Y. Yu, Y. Feng, B. Guan, X.W. Lou, U. Paik, *Energy Environ. Sci.* 9 (2016) 1246–1250.
- [18] L. Wu, Q. Li, C.H. Wu, H. Zhu, A. Mendoza-Garcia, B. Shen, J. Guo, S. Sun, J. Am. Chem. Soc. 137 (2015) 7071–7074.
- [19] Z. Wang, S. Peng, Y. Hu, L. Li, T. Yan, G. Yang, D. Ji, M. Srinivasan, Z. Pan, S. Ramakrishna, J. Mater. Chem. A. 5 (2017) 4949–4961.
- [20] K. Xu, H. Cheng, L. Liu, H. Lv, X. Wu, C. Wu, Y. Xie, *Nano Lett.* 17 (2017) 578–583.
- [21] F.-L. Meng, Z.-L. Wang, H.-X. Zhong, J. Wang, J.-M. Yan, X.-B. Zhang, *Adv. Mater.* 28 (2016) 7948–7955.
- [22] U.I. Kramm, I. Herrmann-Geppert, J. Behrends, K. Lips, S. Fiechter, P. Bogdanoff, J. Am. Chem. Soc. 138 (2016) 635–640.
- [23] Y. Chen, S. Ji, Y. Wang, J. Dong, W. Chen, Z. Li, R. Shen, L. Zheng, Z. Zhuang, D. Wang, Y. Li, *Angew. Chem., Int. Ed.* 56 (2017) 6937–6941.
- [24] S. Li, C. Cheng, X. Zhao, J. Schmidt, A. Thomas, *Angew. Chem., Int. Ed.* 57 (2018) 1856–1862.
- [25] D. Li, B. Ren, Q. Jin, H. Cui, C. Wang, J. Mater. Chem. A. 6 (2018) 2176–2183.
- [26] J. Zhang, L. Dai, *Angew. Chem., Int. Ed.* 55 (2016) 13296–13300.
- [27] W. Wei, H. Liang, K. Parvez, X. Zhuang, X. Feng, K. Müllen, *Angew. Chem., Int. Ed.* 126 (2014) 1596–1600.
- [28] X. Zheng, J. Wu, X. Cao, J. Abbott, C. Jin, H. Wang, P. Strasser, R. Yang, X. Chen, G. Wu, *Appl. Catal. B* 241 (2019) 442–451.
- [29] Q. Jin, B. Ren, D. Li, H. Cui, C. Wang, *Nano Energy* 49 (2018) 14–22.
- [30] B. Ren, D. Li, Q. Jin, H. Cui, C. Wang, J. Mater. Chem. A. 5 (2017) 13196–13203.
- [31] L. Yang, S. Feng, G. Xu, B. Wei, L. Zhang, *ACS Sustainable Chem. Eng.* 7 (2019) 5462–5475.
- [32] H. Liang, F. Meng, M. Cabán-Acevedo, L. Li, A. Forticaux, L. Xiu, Z. Wang, S. Jin, *Nano Lett.* 15 (2015) 1421–1427.
- [33] T.Y. Ma, J. Ran, S. Dai, M. Jaroniec, S.Z. Qiao, *Angew. Chem., Int. Ed.* 54 (2015) 4646–4650.
- [34] X. Liu, L. Wang, P. Yu, C. Tian, F. Sun, J. Ma, W. Li, H. Fu, *Angew. Chem., Int. Ed.* 130 (2018) 16398–16402.
- [35] C.Y. Su, H. Cheng, W. Li, Z.Q. Liu, N. Li, Z. Hou, F.Q. Bai, H.X. Zhang, T.Y. Ma, *Adv. Energy Mater.* 7 (2017) 1602420.
- [36] F. Yang, P. Zhao, X. Hua, W. Luo, G. Cheng, W. Xing, S. Chen, J. Mater. Chem. A. 4 (2016) 16057–16063.
- [37] T.Y. Ma, S. Dai, M. Jaroniec, S.Z. Qiao, J. Am. Chem. Soc. 136 (2014) 13925–13931.
- [38] C.Y. Su, H. Cheng, W. Li, Z.-Q. Liu, N. Li, Z. Hou, F.Q. Bai, H.X. Zhang, T.-Y. Ma, *Adv. Energy Mater.* 7 (2017) 1602420.
- [39] H. Jiang, Y. Yao, Y. Zhu, Y. Liu, Y. Su, X. Yang, C. Li, *ACS Appl. Mater. Interfaces* 7 (2015) 21511–21520.
- [40] L. Song, T. Wang, L. Li, C. Wu, J. He, *Appl. Catal. B* 244 (2019) 197–205.
- [41] B. Guo, Q. Liu, E. Chen, H. Zhu, L. Fang, J.R. Gong, *Nano Lett.* 10 (2010) 4975–4980.
- [42] Z. Liu, Z. Zhao, Y. Wang, S. Dou, D. Yan, D. Liu, Z. Xia, S. Adv. Mater. 29 (2017) 1606207.
- [43] W. Liu, H. Liu, L. Dang, H. Zhang, X. Wu, B. Yang, Z. Li, X. Zhang, L. Lei, S. Jin, *Adv. Funct. Mater.* 27 (2017) 1603904.
- [44] J. Geng, L. Kuai, E. Kan, Q. Wang, B. Geng, *ChemSusChem* 8 (2015) 659–664.